Designing electrode architectures to facilitate electrolyte infiltration for lithium-ion batteries

Abbos Shodiev, Franco M. Zanotto, Jia Yu, Mehdi Chouchane, Jianlin Li, Alejandro A. Franco

▶ **To cite this version:**

Abbos Shodiev, Franco M. Zanotto, Jia Yu, Mehdi Chouchane, Jianlin Li, et al.. Designing electrode architectures to facilitate electrolyte infiltration for lithium-ion batteries. Energy Storage Materials, 2022, 49, pp.268-277. 10.1016/j.ensm.2022.03.049 . hal-03686681

HAL Id: hal-03686681

https://u-picardie.hal.science/hal-03686681v1

Submitted on 20 Jun 2023

HAL is a multi-disciplinary open access archive for the deposit and dissemination of scientific research documents, whether they are published or not. The documents may come from teaching and research institutions in France or abroad, or from public or private research centers.

L'archive ouverte pluridisciplinaire **HAL**, est destinée au dépôt et à la diffusion de documents scientifiques de niveau recherche, publiés ou non, émanant des établissements d'enseignement et de recherche français ou étrangers, des laboratoires publics ou privés.

Distributed under a Creative Commons Attribution 4.0 International License

Energy Storage Materials 49 (2022) 268–277

Contents lists available at ScienceDirect

Energy Storage Materials

journal homepage: www.elsevier.com/locate/ensm

Designing electrode architectures to facilitate electrolyte infiltration for lithium-ion batteries

Abbos Shodiev[a,b,#], Franco M. Zanotto[a,b,#], Jia Yu[a,b], Mehdi Chouchane[a,b], Jianlin Li[c], Alejandro A. Franco[a,b,d,e,*]

[a] Laboratoire de Réactivité et Chimie des Solides (LRCS), CNRS UMR 7314, Université de Picardie Jules Verne, Hub de l'Energie, 15 rue Baudelocque, 80039 Amiens Cedex, France
[b] Réseau sur le Stockage Electrochimique de l'Energie (RS2E), Fédération de Recherche CNRS 3459, Hub de l'Energie, 15 rue Baudelocque, 80039 Amiens Cedex, France
[c] Electrification and Energy Infrastructures Division, Oak Ridge National Laboratory, Oak Ridge, TN 37831, United States
[d] ALISTORE-European Research Institute, Fédération de Recherche CNRS 3104, Hub de l'Energie, 15 rue Baudelocque, 80039 Amiens Cedex, France
[e] Institut Universitaire de France, 103 Boulevard Saint Michel, 75005 Paris, France

ARTICLE INFO

Keywords:
Lithium-ion batteries
Electrode architecture
Electrolyte infiltration
Lattice Boltzmann Method

ABSTRACT

The electrolyte infiltration is a critical step in the Lithium-ion battery (LIB) cell manufacturing process, impacting for instance the solid electrolyte interphase heterogeneity and the cell ageing. The electrolyte infiltration rate and effectivity are tied to the porous mesostructure and dimensions of the electrodes and the separator, which are mainly dictated by electrochemical performance requirements. We propose here the use of architectures with layers of varying pore network properties as a potential approach to tune the wettability of the cell sandwich. We perform infiltration simulations based on the Lattice Boltzmann Method to analyse the electrolyte saturation as a function of time. This descriptor can be used to evaluate different options for cell architectures. We identify porosity, porosity distribution, and particle size distribution of the active material as main experimental variables that allow influencing the electrolyte infiltration process for full cells in an advantageous way. Our modelling framework allows the recommendation of blueprints that reduce the time and energy invested in this critical step of LIB manufacturing.

1. Introduction

Lithium-ion batteries (LIBs) currently power many electronic devices and allow the re-emergence of electric vehicles [1]. Their use is projected to grow as renewable energy sources replace fossil fuels [2]. Therefore, it is necessary to focus on the scalability and cost efficiency of their manufacturing process, as well as improving their general electrochemical performance.

An important step in the manufacturing of LIBs is the introduction of electrolyte in the porous electrode mesostructure. This step constitutes one of the bottlenecks in the overall process [3–9]. It is also important for the final performance to ensure a homogeneous saturation of electrolyte in the pore network, since this allows a continuous path for Li^+ transport [10] and a homogeneous solid electrolyte interphase formation [11]. Recognizing the need for carrying out research in these aspects, several studies have set out to analyse electrolyte percolation through pores in LIB cells. Experimental studies are challenging due to the opacity of the cell components and packaging material, but imaging techniques are evolving and being adapted for *in situ* and *in operando* battery research [12]. Some examples of these techniques applied to the study of electrolyte infiltration use transmission neutron and X-ray imaging [13–15], ultrasound imaging [16], or lock-in thermography experiments [17]. Alternatively, other studies have employed model setups of the electrodes for studying electrolyte flow [12,18]. As a downside, these strategies have low resolution and do not allow a microscopic analysis of how porosity and other electrode properties affect electrolyte flow in the sub-millimetre scale.

The difficulty in performing experiments to acquire reliable and spatially defined data can be partially solved by the use of computational methods. A system like this, in which two phases such as electrolyte and air are in contact within a porous domain, is particularly difficult to model with traditional computational fluid dynamics methods, such as the finite element method, due to their complex boundary geometries and gas-liquid interface dynamics [19]. To cover this and other limitations, the Lattice Boltzmann Method (LBM) was developed [20]. This method considers the simulation domain not as a continuum but as a set of particles occupying discrete positions within a regular lattice.

* Corresponding author.
E-mail address: alejandro.franco@u-picardie.fr (A.A. Franco).
# These authors contributed equally to this work.

https://doi.org/10.1016/j.ensm.2022.03.049
Received 14 January 2022; Received in revised form 2 March 2022; Accepted 28 March 2022
Available online 1 April 2022
2405-8297/© 2022 The Author(s). Published by Elsevier B.V. This is an open access article under the CC BY license (http://creativecommons.org/licenses/by/4.0/)

The fluid behaviour arises as a consequence of successive propagation and collision steps, governed by a particle distribution function. This approach makes it highly parallelizable and allows for the description of liquid-gas and liquid-solid boundary interactions [21–23]. In the energy storage field, this method was already applied for analysing the electrochemistry/fluid dynamics interplay in redox flow batteries [24].

Some previous studies that apply this method for electrolyte infiltration in LIBs were performed by Lee et al. [18,25]. Despite the use of a two-dimensional domain and the consideration of a simplified electrode morphology, these studies demonstrated the capability of LBM for accurately describing electrolyte flow in the porous electrode structures. They showed that LBM was able to represent some key aspects of this process such as the importance of particle shape and compaction. A more recent study, using a model developed by us, extended this approach to three dimensions, including realistic mesostructures extracted from tomography and manufacturing process simulations [10]. This fundamental study highlighted the importance of the pore size and pore network connectivity, which is in turn affected by the calendering step in electrode manufacturing, in the electrolyte impregnation. These factors affect the final wettability and electrochemical performance of the electrodes. A later application of this model focused on the exploration of the parameter space and consequent training of a machine learning model that aimed to reproduce the electrolyte filling dynamics in three dimensions, based on the resolution of the individual pore saturations [26].

Herein, we aim to apply the insights provided by our previously reported electrolyte infiltration model to the smart design of electrode architectures. We propose the porosity, porosity distribution, and particle size distribution of the active material as main experimental variables that allow influencing the electrolyte infiltration process for full cells in an advantageous way. For particular details related to the mesostructure we refer the reader to our previous publication [10]. The objective is to recommend blueprints that reduce the time and energy invested in this critical step of LIB manufacturing.

2. Methods

2.1. Electrode mesostructures generation

The cell mesostructures used as input for the LBM simulations were generated with our *in house* INNOV code [27]. The separator is based on the SEM images from the open-source data of Lagadec and Wood [28] corresponding to a Celgard separator. The same representative 100 μm × 150 μm × 24 μm volume portion was used in all cases. All of the cathode mesostructures are composed of stochastically generated spheres that follow the experimental particle size distribution reported for NMC 111 powder in our previous work [29]. A film-like carbon binder domain in contact with the NMC spheres is also stochastically added, in order to reach a 96:4 mass ratio between active material and CBD. The anode mesostructures were generated in the same way as the cathode, using the same procedure as in one of our previous publications [11], with a particle size distribution fitted to a log-normal probability density function by considering the D10, D50, and D90 values to be 8, 11, and 18 μm, respectively. This follows the particle size distribution of commercial C–NERGY Actilion GHDR 10–4 graphite. The carbon binder domain is also included in the same way as for the cathode, to reach a 96:4 mass ratio between graphite and CBD. All of the electrodes were generated with a cross-section of 100 μm × 100 μm and a thickness of 150 μm. In Sections 3.2 and 3.3, mesostructures generated with different particle sizes are compared. These distributions are arbitrarily generated by shifting the ones presented in the previous paragraph in order to obtain a mean diameter 1.5 times larger or smaller. Each part of the cell was generated with the same cross-section and later attached. In cases where simulations involved electrodes with two layers of different morphologies, each layer was generated independently with half of the intended thickness (50 μm) and then attached without further processing. It should be noted that in terms of LBM simulations, there is no distinction between the CBD, the AM, or the separator domains regarding input parameters such as contact angle. Even if the computational framework can be extended to consider different contact angles for CBD and AM within the electrodes, their experimental local determination remains very challenging.

Table 1
Simulation parameters for LBM simulations.

Parameter	Lattice value	Corresponding physical value
Electrolyte density	10	1300 kg m^{-3}
Gas density	1	130 kg m^{-3}
Contact angle	0.357/1.643	70° [6]
Surface force (gas-liquid)	0.9	7.28 10^{-2} Pa [6]
Δt	1	3.8 10^{-8} s
Reynolds number	10^{-3}	10^{-3}
Capillary number	10^{-5}	10^{-5}
Applied pressure	0.2	202 650 Pa [26]

2.2. Fluid dynamics simulations

Electrolyte infiltration into the porous mesostructure of the cell was modelled in three dimensions according to the Lattice Boltzmann Method (LBM), using the D3Q19 lattice and the BKG collision operator [10,20,30,31]. The distance between adjacent lattice points is 0.66 μm in cells 1 through 7 and 0.50 μm in Cells 8 through 10. Due to numerical limitations of the LBM [32], the maximum density ratio between phases is generally 10; in our simulations, the parameters are chosen to represent a realistic density value for the electrolyte and the lowest possible value for the gas phase. For additional details related to the particular implementation of this method, the reader can refer to our previous publication [10]. The parameters used are summarized in Table 1. These correspond to 1.2 M $LiPF_6$ in ethylene carbonate-diethyl carbonate 3/7 wt% in contact with an NMC532 electrode, as per the values reported in Fig. 2 of reference [6], after conversion to lattice units. The simulations were implemented using the open-source library Palabos version 1.0 [33]. Each simulation took approximately from eight to twenty days, using a server with 256GBs of RAM.

In the initial state, all of the available volume is filled by the lower density phase, representing air. The goal of the simulations is to represent the inflow of electrolyte from a homogeneously distributed upper layer, in the direction parallel to the separator. This represents a cylindrical cell in its conventional infiltration configuration [34]. In our approach, this is considered by fixing the pressure of electrolyte equal to 0.2 lattice units at a thin slice of the system corresponding to $z = 100$ μm. Similarly, the escape of air is taken into account by fixing the air density equal to 1 lattice unit at $z = 0$ μm. The xz planes corresponding to the current collectors at the outer sides of anode and cathode present no-flux boundary conditions, while the yz outer planes present periodic boundary conditions. The acceleration of gravity in the negative z direction is taken into account. Simulations are considered as finished when the maximum change in density for a given lattice point is below an arbitrarily defined threshold of 0.001 lattice units.

The particle density for each of the phases at each lattice point is saved at regular intervals during the simulation. This information was used to obtain the saturation curves in the following way: each lattice point was tagged as filled with electrolyte only if its density for the electrolyte phase is above 0.8; the saturation is defined as the fraction of available lattice points tagged. This procedure can be implemented across the whole domain or only for one of the regions corresponding to the layers that compose the cell.

The visualization of the electrolyte percolation process was performed with Paraview [35] based on the output '.vti' files from the LBM simulations. The electrode structure is shown in blue and the electrolyte is represented in red.

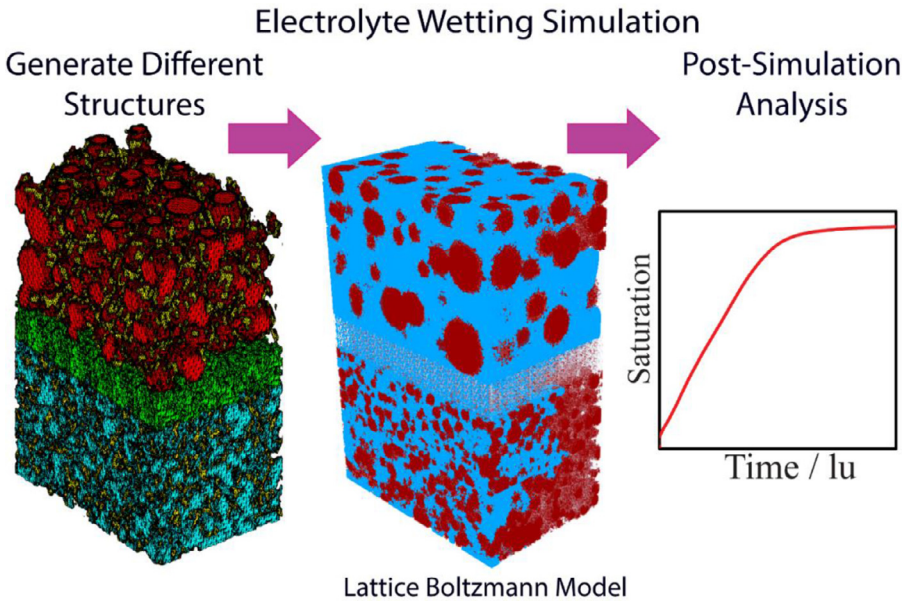

Fig. 1. Schematic representation of the workflow presented in the Methods section and used throughout this work.

In summary, the full workflow presented herein can be schematized as in Fig. 1. Dry electrodes are stochastically generated with the appropriate AM:CBD proportions and particle size distributions. If necessary, the electrodes are generated as two layers and attached. Later, LBM simulations are carried out to evaluate electrolyte flow into the pore network. Finally, saturation curves for either the complete cell or individual layers are constructed from the density at each lattice point.

3. Results and discussion

3.1. Electrolyte infiltration of bi-layer porous electrodes versus homogeneous ones

Recently, it has been demonstrated that electrode architecture has a significant impact on rate performance [36,37]. For instance, a two-layer electrode with appropriate configurations of particle size and porosity rendered 2X improvement at 2C discharge capacity compared to the worst configurations [38]. The main hypothesis in our work is that the use of carefully designed mixed-porosity electrodes can also improve the electrolyte infiltration process. This improvement can be assessed mainly through two variables: final saturation and time required to reach it. In order to test this hypothesis, we performed simulations for the geometries schematized in Fig. 2A. Each electrode in cells 1 and 3 presents the same 32% overall porosity, which is common for application. The same is true for cells 2 and 4 with an overall porosity of 42%. The difference lies in its distribution: in the first two cases the region closest to the separator is more porous than the region closest to the current collectors. This porosity distribution is in accordance to previous studies [36,37] which show that electrodes for which a more porous fraction is closest to the separator present some advantages in terms of electrochemical behaviour with respect to the opposite configuration.

The overall electrolyte saturation curves for these four systems are shown in Fig. 2B. When comparing cells 1 and 3, with 32% overall porosity, the advantage of a heterogeneous electrode mesostructure is clearly revealed. Both the final saturation and the saturation rate are higher for cell 1. This result contrasts with the close resemblance of the saturation curves for cells 2 and 4. Comparing the latter cases, the heterogeneous mesostructure still presents a higher final saturation and initial saturation rate, albeit with a much smaller difference to cell 4. In light of these results, it is possible to conclude that a central layer of higher porosity can improve not only the electrochemical characteristics of a cell [36,37], but also the crucially time-consuming step of electrolyte impregnation. This trend becomes much more important for lower porosity mesostructures, for which electrolyte percolation is harder.

To analyse this result in more detail, it is useful to observe each part of the electrodes independently. Fig. 3 shows the electrolyte within the pores during the infiltration process. It can be seen that the more porous layers act as a more efficient conduit for the liquid phase. The resulting flow from the more porous layers to the less porous adjacent layers increases the overall saturation rate. Fig. 3 also shows that in general the anode fills more quickly than the cathode. As discussed in our previous work [10], a final saturation value lower than one is expected, particularly for mesostructures with lower porosity, due to the presence of inaccessible regions which remain filled with air. For this reason, it is expected that these snapshots also show more pockets of air remaining after infiltration. Although this is difficult to discern, a final saturation lower than one can be seen in the plots corresponding to the time evolution of saturation.

Fig. 4 shows the saturation as a function of time for the different electrodes that compose cells 1 through 4. These plots show that in all cases, graphite anodes fill faster and to a larger extent than NMC cathodes. This is the expected trend, as the mean particle size is shifted towards larger values in graphite. This yields larger and less isolated pores, which are filled more quickly [10]. Both panels in Fig. 4 show that the two-layer approach is beneficial for infiltration in both cathode and anode, regardless of overall porosity. As before, the difference is more prominent when the electrode is relatively less porous. In addition, the cathode, with its lower mean particle size shows a larger difference between cells 1 and 3, with their relatively low porosity.

The contribution of each layer to the saturation curves can be resolved as shown in Fig. 5. We focus our analysis in cells 1 and 3. The corresponding plots for cells 2 and 4 are presented in the Supporting Information section, and show similar but less marked trends. As expected, the equally porous layers that form cell 3 do not differ too much. In the case of the two-layer cathode configuration (cell 1), the highly porous layer closest to the separator fills at the highest rate. Interestingly, the compact layer near the current collector fills at a rate comparable with the more porous layers in the homogeneous electrode. In this lies the advantage of this approach: the presence of a very permeable layer greatly accelerates the infiltration in the contiguous layers, acting as a reservoir from which lateral flow occurs. This effect is equally important in the anode. However, its effect is less significant because, as discussed before, the anode is not the limiting factor in the homogeneous porosity case.

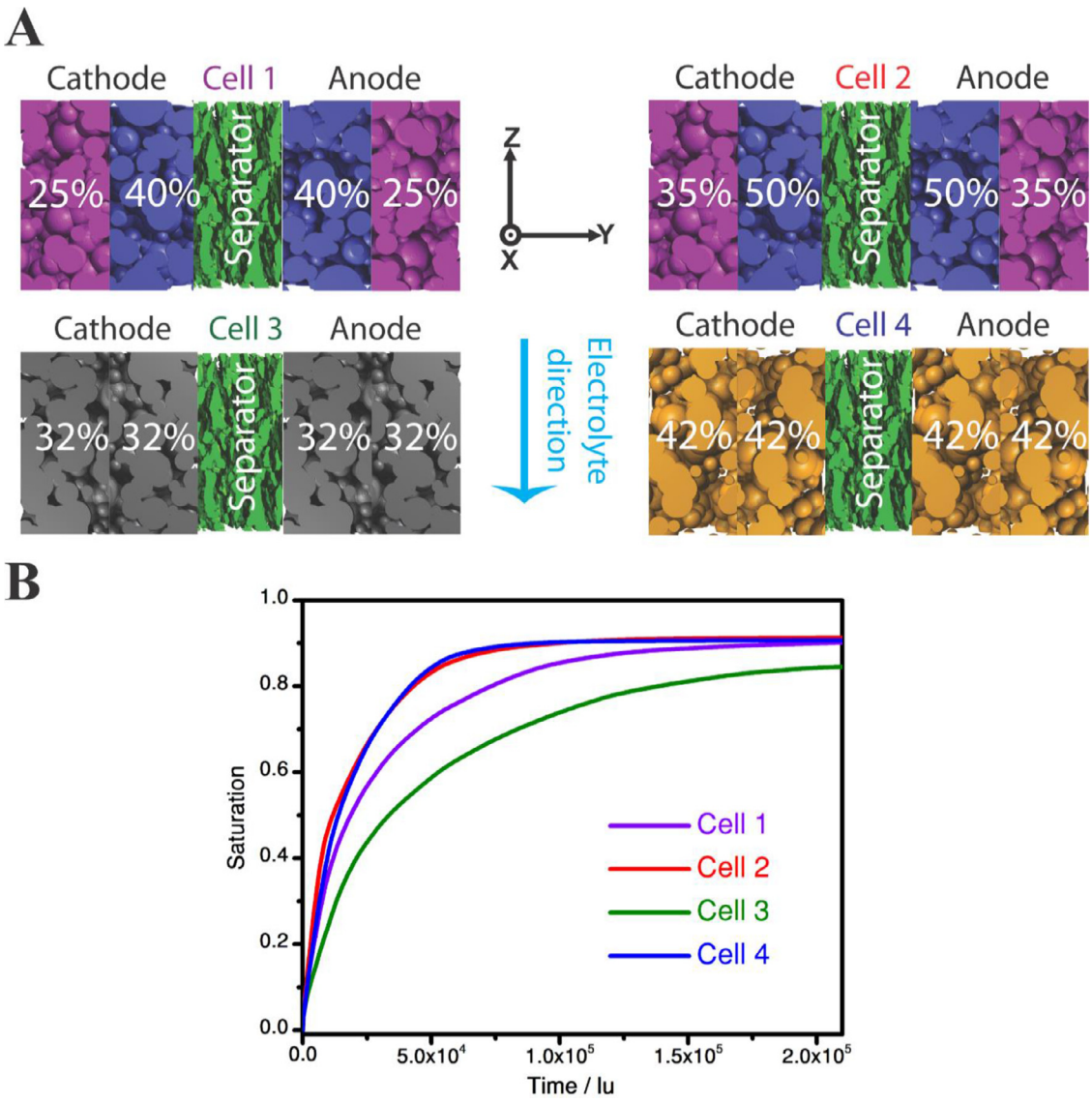

Fig. 2. (A) Schematic representation of the four cells studied in this subsection. The electrolyte flow is in the negative z direction, as well as the acceleration of gravity. The percentages in white on each layer correspond to the porosity values. (B) Overall saturation values as a function of time each of the cells presented in panel A. The electrolyte volumes corresponding to the final saturation value are: 1.05×10^6 μm^3 (cell 1), 1.35×10^6 μm^3 (cell 2), 1.02×10^6 μm^3 (cell 3), 1.34×10^6 μm^3 (cell 4).

Lastly, it is possible to perform the same analysis for the separator, as shown in Fig. 6. The input mesostructure for this layer was adapted from tomographic data from a Celgard separator [28] and presents a porosity of 40%. This relatively high value translates in a quick infiltration process, particularly in comparison with the cathode. It should be noted that in all of these cases the separator phase is identical. In consequence, all differences can be attributed to the adjacent layers structures. Experimental studies have focused on the particular effect of the separator in infiltration rate, [17] which the present model would also be able to describe.

Since this layer does not represent a limiting step, its saturation curve is relatively insensitive to the surrounding electrodes porosities. It can be clearly noticed, though, that in cell 2, when this layer is surrounded by layers with a high porosity value of 50%, saturation is the fastest. On the contrary, when this layer is surrounded by layers with a relatively low porosity of 32%, its saturation is the slowest, as it is mostly contributing as a channel for the flow of electrolyte to the neighbouring layers on both sides.

3.2. Layered cells with variations in particle size distribution

In the previous subsection, we have analysed the effect of porosity and its distribution along the cell in the electrolyte infiltration process. However, we also assigned the differences observed between saturation in anode and cathode to their different particle size distributions. In addition, the pore network is an important factor, as demonstrated in our previous publication [10]. Thus, the use of more than one layer with different particle sizes becomes a potentially useful tool for optimizing electrolyte infiltration. Aiming to test this assertion, we generated two arbitrary additional distributions. Starting from the experimental data for both anode and cathode, (in grey line in Fig. 7A), the two others are the result of shifting them towards larger (in violet) and smaller (in blue) radii. These are labelled “Experimental”, “Large”, and “Small”, respectively. We then generated three new cell architectures, as presented in Fig. 7B. In all cases, the porosity of each layer that forms these electrodes is 35%, but the particle sizes vary.

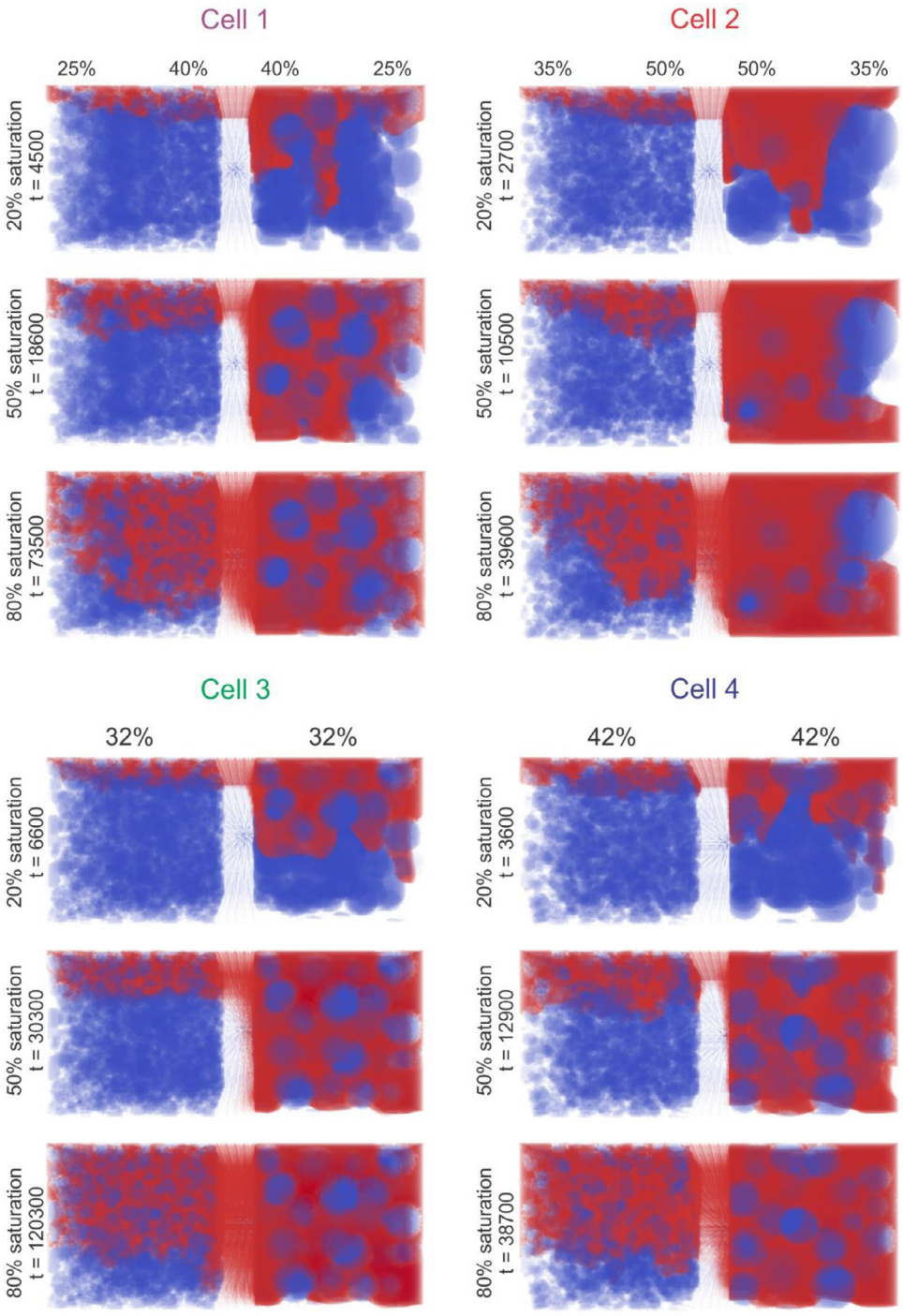

Fig. 3. (A) Snapshots of the simulation domain at set stages during infiltration (20%, 50% and 80% of the empty space occupied by electrolyte) corresponding to cells 1 through 4. The timestep values are all informed in lattice units. The solid components of the cell are represented in partially transparent blue colour, while the electrolyte is shown in red colour. The percentage values on top of the cells correspond to the porosity of the layers. It should be noted that different saturation rates do not necessarily correspond to the same time since the start of the simulation.

The saturation curves presented in Fig. 7C show a noticeable increase in saturation rate when the particle size distribution is heterogeneous throughout the electrode, as in cells 5 and 7, with respect to the homogeneous distribution in cell 6. This effect can be explained in an analogous way to the trends observed for cells 1 through 4: the faster flow throughout the larger particle sized layers contributes to the infiltration in the smaller particle sized contiguous layer. The comparison between snapshots corresponding to the same timestep for all three cells in panel D confirms this, as the electrolyte-air limits are always further down for the layers with larger particle sizes. Figure S2 in the supporting information details the time evolution of saturation in each layer of these cells. In contrast, the presence of a layer with smaller mean particle size in cells 5 and 7 creates more isolated pockets that remain unfilled, yielding a final saturation value lower than one.

Lastly, the similarity between the saturation curves for cells 5 and 7 indicates that the particular order in which the layers are stacked does not have a significant effect, as long as the overall porosities are maintained. It should be noted that this insight applies only for the impregnation step in the cell manufacturing process. Hence, the study of the electrochemical performance of these two architectures would be necessary for a complete analysis, allowing for an optimal choice of electrode mesostructures.

It should be noted that although these results might suggest that increasing the particle size distribution of the active material is always

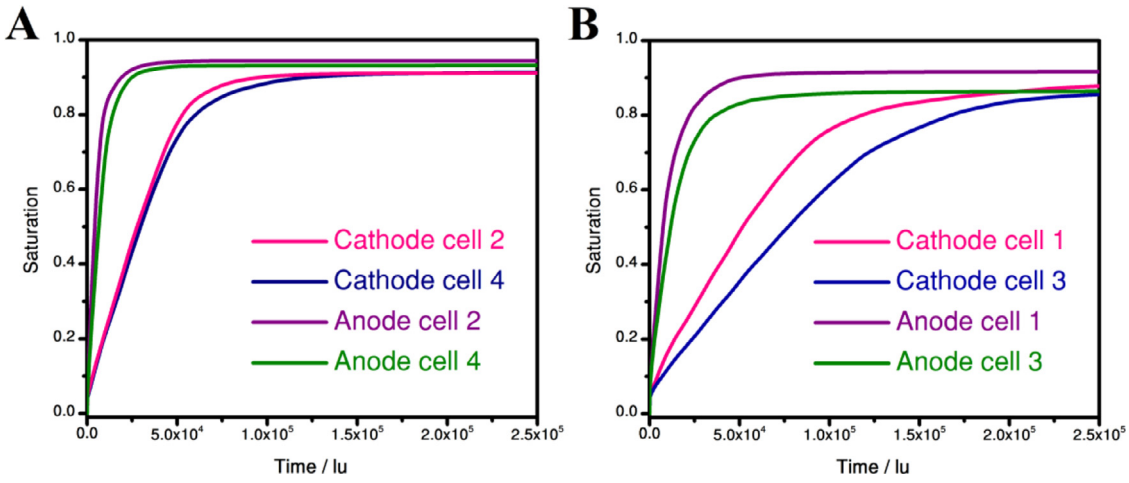

Fig. 4. Saturation curves for each electrode schematized in Fig. 2A. (A) Comparison between electrodes with 42% porosity. (B) Comparison between electrodes with 32% porosity.

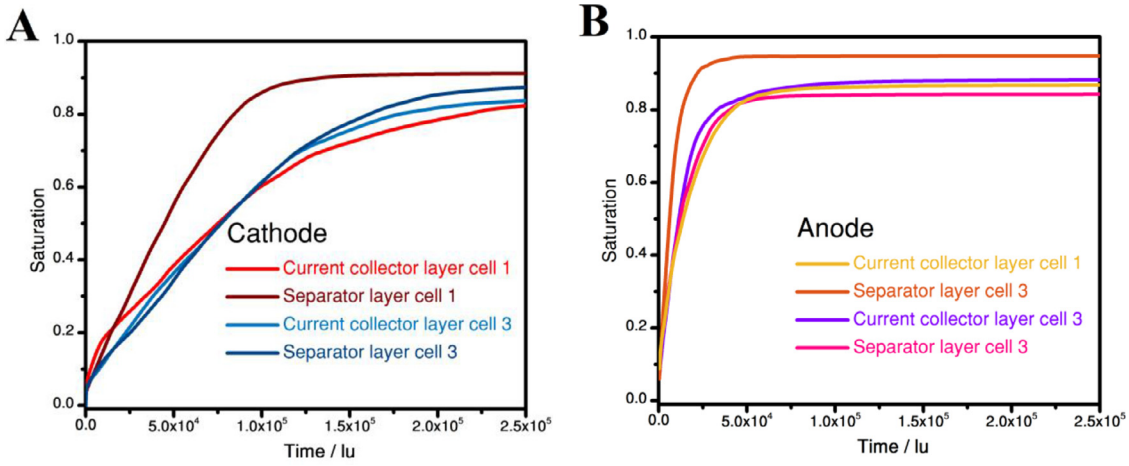

Fig. 5. Saturation curves for each layer in cells 1 and 3. (A) Comparison between cathode layers. (B) Comparison between the anode layers. The reader can refer to Figure S1 in the Supporting Information for the corresponding plots for cells 2 and 4.

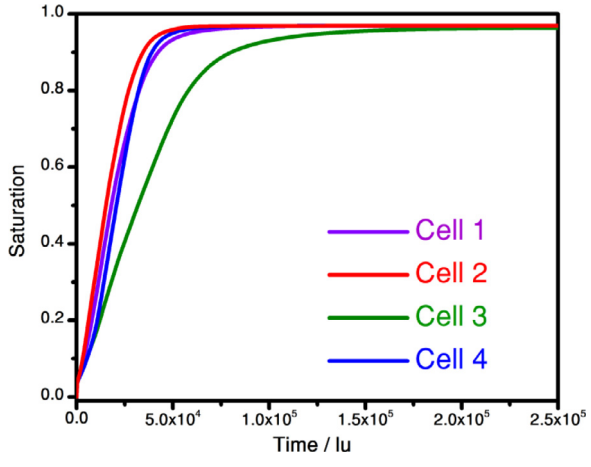

Fig. 6. Saturation curves for each separators in cells 1 through 4.

convenient for speeding up electrolyte infiltration, this can reduce the electrochemical performance of the battery. For this reason, we propose that fluid dynamics simulations for electrolyte infiltration are useful as long as they are complemented by simulations describing additional aspects of the manufacturing process, as well as electrochemical characterization [39].

3.3. Designing heterogeneous electrode architectures with layered porosity and particle size distribution

From the previous sections we can conclude that for a given global electrode porosity, an heterogeneous distribution in a two-layer configuration significantly increases the saturation rate. Also, a layered architecture in terms of mean particle size presents notable advantages. These two strategies can be combined to maximise the saturation rate and final saturation. In the present section, we study three cells in layered configurations with the goal of predicting an optimal configuration.

Fig. 8A shows schematic representations of the model architectures. In all cases, the inner layers closest to the separator are more porous than the outer layers, following the conclusions from subsection 3.1. As before, the labels “Large” and “Small” are a reference to the particle size distributions in Fig. 7A.

Cell 8 presents larger particles in the higher porosity layer of the cathode and in the lower porosity layer of the anode. Cell 10 presents the opposite configuration, where the larger particle sizes are located in the lower porosity layer for the cathode and in the higher porosity layer for the anode. Panel B shows a significantly higher saturation rate for the former case. The saturation curve for the intermediate case (cell 9) falls between these two extremes. Fig. 8B by itself would suggest that the most convenient strategy would be to use a larger mean particle size in the more porous layer in the cathode and a larger mean size for the less porous layer in the anode. This increases saturation rate considerably

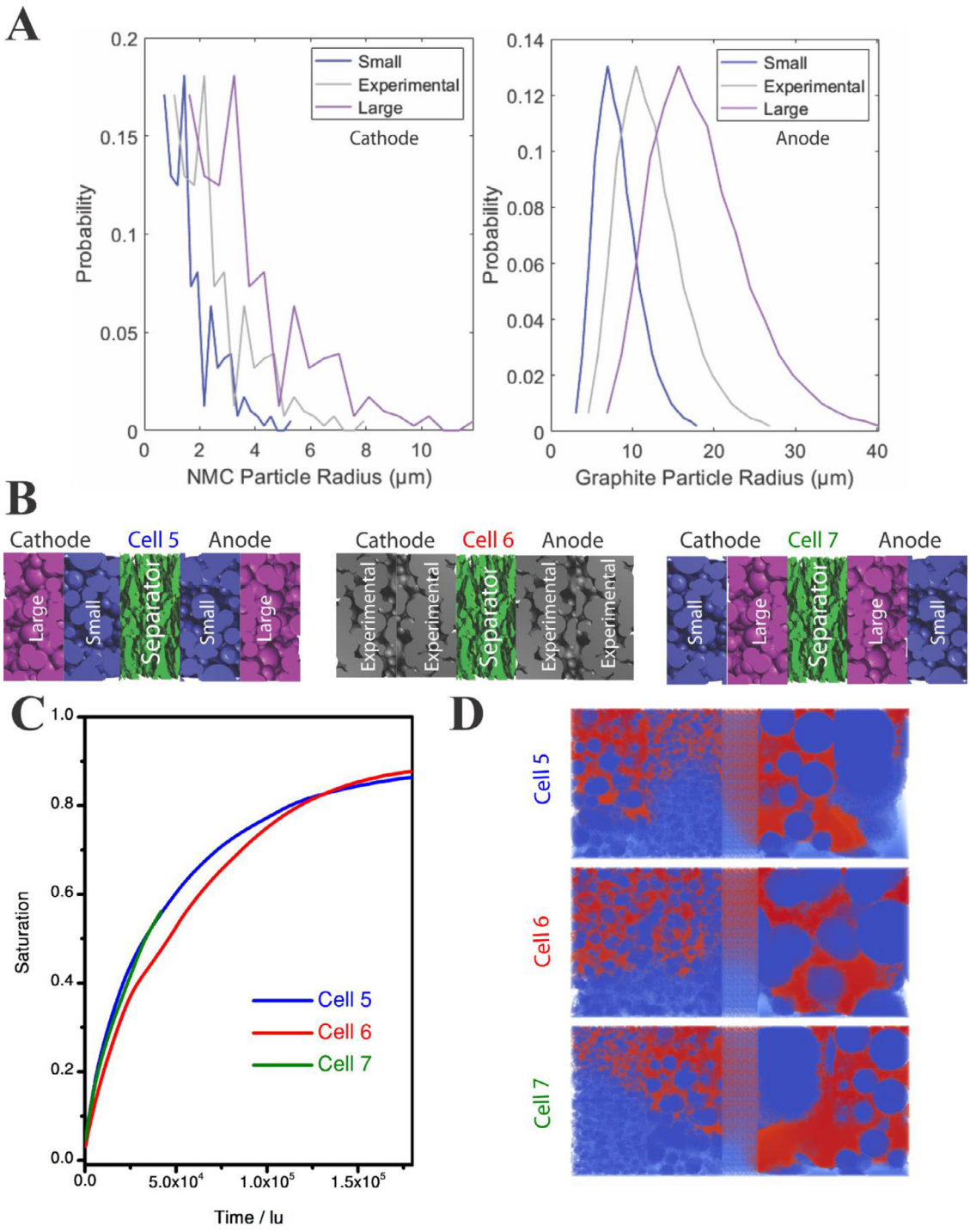

Fig. 7. (A) Normalized particle size distribution of active material in stochastically generated NMC cathodes (left) and graphite anodes (right). The grey curves represent the experimental values and the rest are generated by shifting the original towards larger or smaller values. (B) Schematic representations of cells 5 through 7 analysed in this section. In all cases the porosity of each electrode is 35%. The label and colour on each layer represents the particle size distribution used for its generation. (C) Overall saturation as a function of time for the cells presented in panel B. The electrolyte volumes corresponding to the final saturation values are: 1.08×10^6 μm^3 (cell 5), 1.07×10^6 μm^3 (cell 6), and 1.09×10^6 μm^3 (cell 7). (D) Snapshots corresponding to $t = 108{,}300$ lu during the LBM simulations corresponding to cells 5 through 7. Videos showing the electrolyte movement within the porous structure of cells 5 and 6 can be found as part of the Supporting Information.

and maintains the final saturation value. However, it is unclear from this plot why the opposite strategies produce the same trend in anode and cathode.

To investigate further, it is possible to analyse the individual saturation curves for each layer in cells 8 through 10, as shown in Fig. 9. Panel A, corresponding to cell 8, shows a sharp increase in the saturation for all of the layers except, notably, the cathode layer corresponding to the current collector side. This particular layer has a porosity of only 25% and the smallest mean particle size in the cell. This translates to a very slow electrolyte infiltration and low final saturation value for this layer. In short, the saturation curve for cell 8 is driven largely by the quick infiltration for all of the remaining layers, but the slow and incomplete

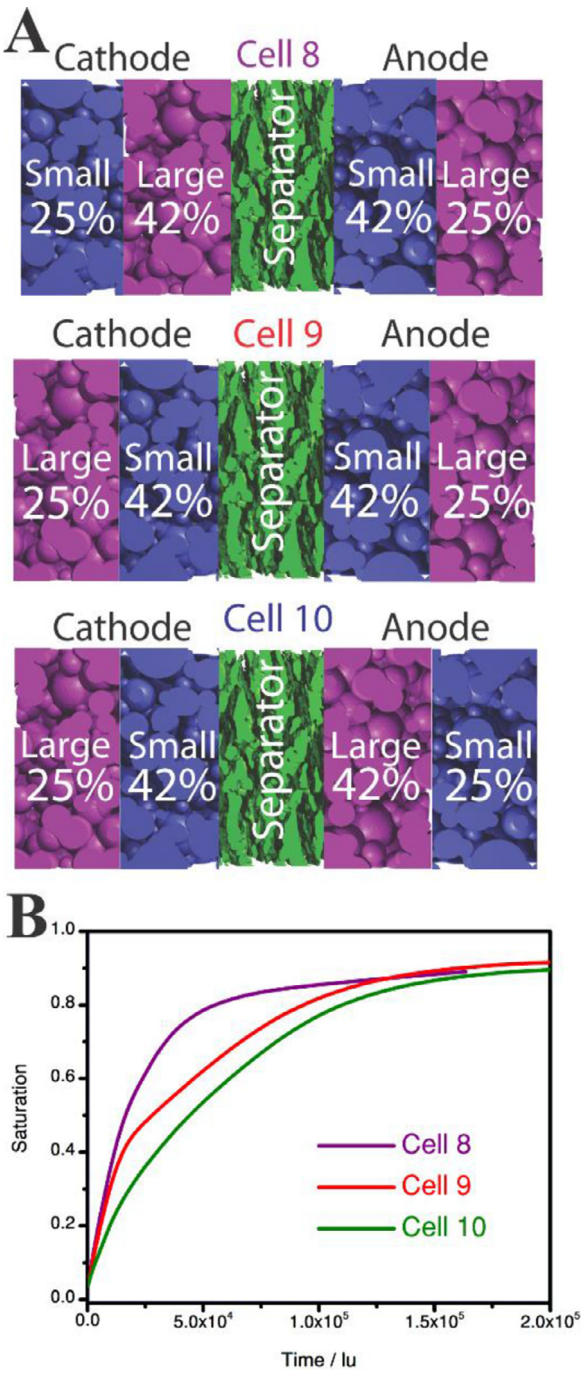

Fig. 8. (A) Schematic representations of cells 8 through 10 analysed in this section. The label on each layer represents the particle size distribution and the porosity used for its generation. (B) Overall saturation as a function of time for the cells presented in panel A. The electrolyte volumes corresponding to the final saturation values are: 1.02×10^6 μm^3 (cell 8), 1.05×10^6 μm^3 (cell 9), and 1.02×10^6 μm^3 (cell 10).

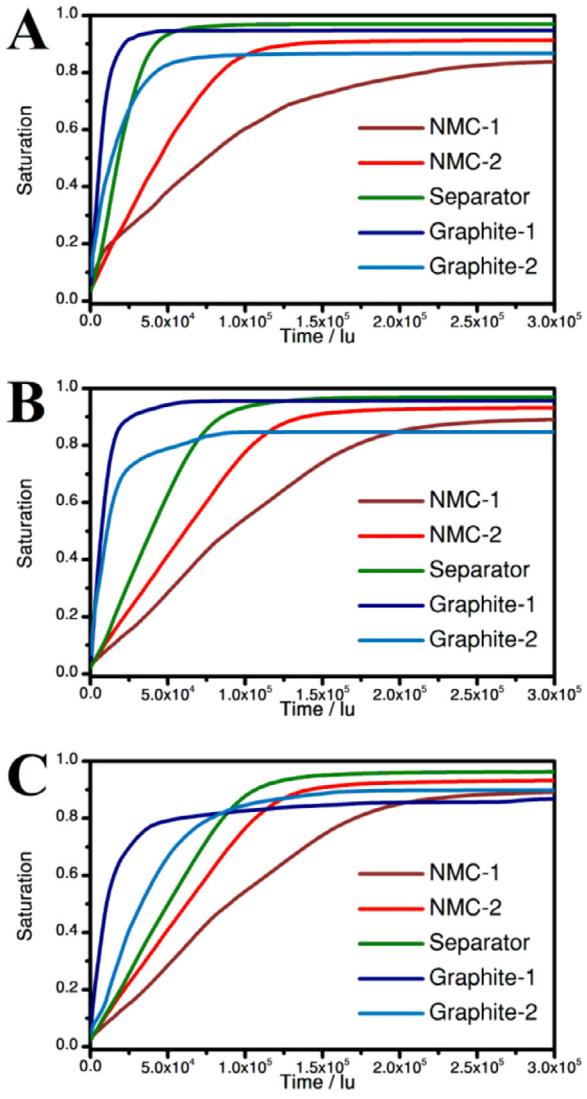

Fig. 9. Saturation curves corresponding to each of the layers that compose cells 8 through 10. (A) Cell 8. (B) Cell 9. (C) Cell 10.

flow through this cathode layer makes this architecture less suitable for actual use. The reverse case in cell 10 presents the slowest saturation process. Fig. 9C shows that the low porosity layer in the cathode continues to be the bottleneck of the percolation process, though its larger mean particle size allows for a higher saturation rate.

As a final point of interest, the anode layers in cell 8 (Fig. 9A) and cell 9 (Fig. 9B), which are identical, present very similar profiles. The same holds true for the cathode layers in cell 9 and cell 10 (Fig. 9C). This evidences the limited net flow between electrodes across the separator, which can be attributed to the high relative porosity of the chosen Celgard separator. Additional studies with different separator mesostructures might help clarify this point, though this is beyond the scope of this work.

In conclusion, simulations for cells 8–10 highlight a complex tradeoff between porosity and particle size distribution heterogeneities along the electrode thickness as factors impacting the cell wettability. This tradeoff hinders the extraction of simple guidelines for minimizing time and cost of impregnation. However, this simulation step can be of great use as part of a series that aims to simulate the totality of the manufacturing process [39].

4. Conclusion

Electrolyte infiltration is a costly and time-consuming stage in the manufacturing of lithium ion batteries. In this work, we use a time-dependant 3D LBM model of this process that allows to identify important variables that greatly influence saturation rate and final saturation. This model solves for the fluid dynamics of a liquid phase as it wets the porous electrode mesostructure, considering the interaction between walls and liquid and a second phase that represents the air,

initially present within the pores. In our previously reported work, we showed that the final saturation has a noticeable effect on electrochemical performance [10]. Porosity, pore size distribution, tortuosity factor and pore network connectivity play a crucial role in the saturation and in the time required to reach it.

The work presented here focuses on using this model and the insight it provides to design novel electrode architectures that maximise saturation rate during the electrolyte filling, by minimizing losses in the overall electrochemical performance. The two main tools at our disposal are the distribution in different layers of an electrode of porosity and particle size distribution of the active material. Other parameters such as the type of electrolyte and separator, and surface area of the porous structure will also affect how electrolyte spreads into cells. While we have not analysed all of them, the model can be straightforwardly extended to different structures morphologies, regardless of their origin (either from experimental data, physics-based models, stochastically generated, or others), and even different materials, as long as the viscosity, density and contact angle are known.

Our findings indicate that a heterogeneous distribution of porosity in both electrodes presents clear advantages with respect to a homogeneous mesostructure with the same overall porosity. This architecture is compatible with a suitable electrochemical performance [36,37]. Furthermore, the advantages of this approach become more important for less porous mesostructures. The use of active material with different particle size distributions is a different tool that allows to tune the connectivity of the pore network, and also can be used in a similar approach: two layers with different mean particle sizes allow the electrolyte impregnation to proceed faster than an electrode with an intermediate mean particle size. Both of these results can be attributed to the importance of the lateral flow from more permeable layers, which are filled first, to less permeable ones. Finally, our model also shows that the combination of these two strategies requires some careful consideration of the permeability of the individual layers along with the whole cell.

The work presented here highlights the impact of the textural properties of the LIB cell sandwich on the electrolyte infiltration dynamics and the consequent cell wettability. Our study stresses about complex tradeoffs between porosity distribution along the anode and the cathode electrode thicknesses as well as active material particle size distribution within them. This calls for engineering strategies at the cell sandwich design level to facilitate the electrolyte wetting, but without removing attention from the electrochemical performances that those architectures may deliver in practical applications.

This computational modelling approach opens further pathways for future and more complete studies. For example, the impact of uneven wettability of the electrode on the formation of solid electrolyte interphase will be assessed by us in the near future. In another page, we are constrained on the size of the simulation domains, which are still far from the actual experimental system. The saturation time does not necessarily increase in a linear way as the system increases in size, which hinders the formulation of predictions regarding experimental systems. Furthermore, the calculation times are in the order of hours to days. For these reasons, we are confident that the use of machine learning tools, proven by us to be very effective at predicting saturation curves, [26] will drastically decrease calculation times, allowing for the study of real-size cells and the prediction of saturation curves in the order of seconds. In this way, a practical tool for experimentalists could be generated, to greatly accelerate the optimization of electrode wetting and electrolyte/active material interfaces in LIBs.

Declaration of Competing Interest

The authors declare that they have no known competing financial interests or personal relationships that could have appeared to influence the work reported in this paper.

CRediT authorship contribution statement

Abbos Shodiev: Methodology, Software, Investigation, Writing – review & editing, Visualization. **Franco M. Zanotto:** Validation, Formal analysis, Data curation, Writing – original draft, Visualization. **Jia Yu:** Validation, Formal analysis, Data curation, Writing – review & editing, Visualization. **Mehdi Chouchane:** Software, Writing – review & editing. **Jianlin Li:** Conceptualization, Writing – review & editing, Supervision. **Alejandro A. Franco:** Methodology, Conceptualization, Resources, Writing – review & editing, Supervision, Project administration, Funding acquisition.

Acknowledgements

A.S. and F.M.Z. contributed equally to this work. A.A.F., A.S., and M.C. acknowledge the European Union's Horizon 2020 research and innovation program for the funding support through the European Research Council (grant agreement 772873, "ARTISTIC" project). A.A.F. and J. Y. acknowledge the funding of the European project SONAR, under the grant agreement 875489. A.A.F. and F.M.Z. acknowledge the European Union's Horizon 2020 research and innovation program under grant agreement No 957189 (BIG-MAP). J. L. appreciates the support from the Office of Energy Efficiency and Renewable Energy (EERE) Vehicle Technologies Office (VTO). The research at Oak Ridge National Laboratory (ORNL) is managed by UT Battelle, LLC, for the U. S. Department of Energy (DOE) under contract DE-AC05–00OR22725. A.A.F. acknowledges Institut Universitaire de France for the support.

Supplementary materials

Supplementary material associated with this article can be found, in the online version, at doi:10.1016/j.ensm.2022.03.049.

References

[1] A.A. Franco, A. Rucci, D. Brandell, C. Frayret, M. Gaberscek, P. Jankowski, P. Johansson, Boosting rechargeable batteries R&D by multiscale modeling: myth or reality? Chem. Rev. 119 (2019) 4569–4627, doi:10.1021/acs.chemrev.8b00239.
[2] D. Larcher, J.-.M. Tarascon, Towards greener and more sustainable batteries for electrical energy storage, Nat. Chem. 7 (2015) 19–29, doi:10.1038/nchem.2085.
[3] D.L. Wood, J. Li, C. Daniel, Prospects for reducing the processing cost of lithium ion batteries, J. Power Sources. 275 (2015) 234–242, doi:10.1016/j.jpowsour.2014.11.019.
[4] T. Knoche, F. Surek, G. Reinhart, A Process Model for the Electrolyte Filling of Lithium-ion Batteries, Procedia CIRP 41 (2016) 405–410, doi:10.1016/j.procir.2015.12.044.
[5] D.L. Wood, J. Li, S.J. An, Formation Challenges of Lithium-Ion Battery Manufacturing, Joule 3 (2019) 2884–2888, doi:10.1016/j.joule.2019.11.002.
[6] A. Davoodabadi, J. Li, Y. Liang, D.L. Wood, T.J. Singler, C. Jin, Analysis of electrolyte imbibition through lithium-ion battery electrodes, J. Power Sources. 424 (2019) 193–203, doi:10.1016/j.jpowsour.2019.03.115.
[7] J. Li, J. Fleetwood, W.B. Hawley, W. Kays, From Materials to Cell: state-of-the-Art and Prospective Technologies for Lithium-Ion Battery Electrode Processing, Chem. Rev. (2021) acs.chemrev.1c00565. https://doi.org/10.1021/acs.chemrev.1c00565.
[8] A. Davoodabadi, J. Li, H. Zhou, D.L. Wood, T.J. Singler, C. Jin, Effect of calendering and temperature on electrolyte wetting in lithium-ion battery electrodes, J. Energy Storage. 26 (2019) 101034, doi:10.1016/j.est.2019.101034.
[9] A. Davoodabadi, C. Jin, D.L. Wood III, T.J. Singler, J. Li, On electrolyte wetting through lithium-ion battery separators, Extrem. Mech. Lett. 40 (2020) 100960, doi:10.1016/j.eml.2020.100960.
[10] A. Shodiev, E. Primo, O. Arcelus, M. Chouchane, M. Osenberg, A. Hilger, I. Manke, J. Li, A.A. Franco, Insight on electrolyte infiltration of lithium ion battery electrodes by means of a new three-dimensional-resolved lattice Boltzmann model, Energy Storage Mater 38 (2021) 80–92, doi:10.1016/j.ensm.2021.02.029.
[11] M. Chouchane, O. Arcelus, A.A. Franco, Heterogeneous solid-electrolyte interphase in graphite electrodes assessed by 4D-Resolved computational simulations, Batter. Supercaps. 4 (2021) 1457–1463, doi:10.1002/batt.202100030.
[12] Z. Deng, X. Lin, Z. Huang, J. Meng, Y. Zhong, G. Ma, Y. Zhou, Y. Shen, H. Ding, Y. Huang, Recent progress on advanced imaging techniques for lithium-ion batteries, Adv. Energy Mater. 11 (2021) 2000806, doi:10.1002/aenm.202000806.
[13] T. Knoche, V. Zinth, M. Schulz, J. Schnell, R. Gilles, G. Reinhart, In situ visualization of the electrolyte solvent filling process by neutron radiography, J. Power Sources. 331 (2016) 267–276, doi:10.1016/j.jpowsour.2016.09.037.

[14] A. Schilling, P. Gümbel, M. Möller, F. Kalkan, F. Dietrich, K. Dröder, X-ray based visualization of the electrolyte filling process of lithium ion batteries, J. Electrochem. Soc. 166 (2019) A5163–A5167, doi:10.1149/2.0251903jes.
[15] A. Davoodabadi, J. Li, Y. Liang, R. Wang, H. Zhou, D.L. Wood, T.J. Singler, C. Jin, Characterization of surface free energy of composite electrodes for lithium-ion batteries, J. Electrochem. Soc. 165 (2018) A2493–A2501, doi:10.1149/2.0341811jes.
[16] D. Zhe, H. Zhenyu, L. Lei, S. Yunhui, Applications of ultrasound technique in characterization of lithium-ion batteries, Energy Storage Sci. Technol. 8 (2019) 1033–1039, doi:10.12028/j.issn.2095-4239.2019.0146.
[17] A. Schilling, S. Wiemers-Meyer, V. Winkler, S. Nowak, B. Hoppe, H.H. Heimes, K. Dröder, M. Winter, Influence of Separator Material on Infiltration Rate and Wetting Behavior of Lithium-Ion Batteries, Energy Technol 8 (2020) 1900078, doi:10.1002/ente.201900078.
[18] S.G. Lee, D.H. Jeon, B.M. Kim, J.H. Kang, C.-J. Kim, Lattice Boltzmann simulation for electrolyte transport in porous electrode of lithium ion batteries, J. Electrochem. Soc. 160 (2013) H258–H265, doi:10.1149/2.017306jes.
[19] A. Narváez, K. Yazdchi, S. Luding, J. Harting, From creeping to inertial flow in porous media: a lattice Boltzmann–finite element study, J. Stat. Mech. Theory Exp. 2013 (2013) P02038, doi:10.1088/1742-5468/2013/02/P02038.
[20] X. Shan, H. Chen, Lattice Boltzmann model for simulating flows with multiple phases and components, Phys. Rev. E. 47 (1993) 1815–1819, doi:10.1103/PhysRevE.47.1815.
[21] S. Takenaka, K. Suga, T. Kinjo, S. Hyodo, Flow simulations in a sub-micro porous medium by the lattice boltzmann and the molecular dynamics methods, in: ASME 2009 7th Int. Conf. Nanochannels, Microchannels Minichannels, ASMEDC, 2009, pp. 927–936, doi:10.1115/ICNMM2009-82062.
[22] E.M. Viggen, The Lattice Boltzmann method: Fundamentals and Acoustics, Norwegian University of Science and Technology, 2014.
[23] L. Chen, Q. Kang, Y. Mu, Y.-L. He, W.-Q. Tao, A critical review of the pseudopotential multiphase lattice Boltzmann model: methods and applications, Int. J. Heat Mass Transf. 76 (2014) 210–236, doi:10.1016/j.ijheatmasstransfer.2014.04.032.
[24] D. Zhang, Q. Cai, O.O. Taiwo, V. Yufit, N.P. Brandon, S. Gu, The effect of wetting area in carbon paper electrode on the performance of vanadium redox flow batteries: a three-dimensional lattice Boltzmann study, Electrochim. Acta. 283 (2018) 1806–1819, doi:10.1016/j.electacta.2018.07.027.
[25] S.G. Lee, D.H. Jeon, Effect of electrode compression on the wettability of lithium-ion batteries, J. Power Sources. 265 (2014) 363–369, doi:10.1016/j.jpowsour.2014.04.127.
[26] A. Shodiev, M. Duquesnoy, O. Arcelus, M. Chouchane, J. Li, A.A. Franco, Machine learning 3D-resolved prediction of electrolyte infiltration in battery porous electrodes, J. Power Sources. 511 (2021) 230384, doi:10.1016/j.jpowsour.2021.230384.
[27] M. Chouchane, A. Rucci, A.A. Franco, A versatile and efficient voxelization-based meshing algorithm of multiple phases, ACS Omega 4 (2019) 11141–11144, doi:10.1021/acsomega.9b01279.
[28] M.F. Lagadec, V. Wood, Microstructure of Celgard® PP1615 Lithium-Ion Battery separator, (2018). https://doi.org/10.3929/ethz-b-000265085.
[29] A.C. Ngandjong, T. Lombardo, E.N. Primo, M. Chouchane, A. Shodiev, O. Arcelus, A.A. Franco, Investigating electrode calendering and its impact on electrochemical performance by means of a new discrete element method model: towards a digital twin of Li-Ion battery manufacturing, J. Power Sources. 485 (2021) 229320, doi:10.1016/j.jpowsour.2020.229320.
[30] Y.H. Qian, D. D'Humières, P. Lallemand, Lattice BGK models for Navier-Stokes equation, Europhys. Lett. 17 (1992) 479–484, doi:10.1209/0295-5075/17/6/001.
[31] D. Arumuga Perumal, A.K. Dass, A review on the development of lattice Boltzmann computation of macro fluid flows and heat transfer, Alexandria Eng. J. 54 (2015) 955–971, doi:10.1016/j.aej.2015.07.015.
[32] T. Inamuro, T. Ogata, S. Tajima, N. Konishi, A lattice Boltzmann method for incompressible two-phase flows with large density differences, J. Comput. Phys. 198 (2004) 628–644, doi:10.1016/j.jcp.2004.01.019.
[33] J. Latt, O. Malaspinas, D. Kontaxakis, A. Parmigiani, D. Lagrava, F. Brogi, M. Ben, Y. Belgacem, S. Thorimbert, S. Leclaire, F. Li, J. Marson, C. Lemus, R. Kotsalos, C. Conradin, R. Coreixas, F. Petkantchin, J. Raynaud, B. Beny, Chopard, Palabos: parallel lattice boltzmann solver, Comput. Math. with Appl 81 (2021) 334–350, doi:10.1016/j.camwa.2020.03.022.
[34] F.J. Günter, S. Rössler, M. Schulz, W. Braunwarth, R. Gilles, G. Reinhart, Influence of the cell format on the electrolyte filling process of lithium-ion cells, Energy Technol 8 (2020) 1801108, doi:10.1002/ente.201801108.
[35] U. Ayachit, The ParaView Guide: A Parallel Visualization Application, Kitware, 2015.
[36] S. Kalnaus, K. Livingston, W.B. Hawley, H. Wang, J. Li, Design and processing for high performance Li ion battery electrodes with double-layer structure, J. Energy Storage. 44 (2021) 103582, doi:10.1016/j.est.2021.103582.
[37] C. Huang, N.P. Young, J. Zhang, H.J. Snaith, P.S. Grant, A two layer electrode structure for improved Li Ion diffusion and volumetric capacity in Li Ion batteries, Nano Energy 31 (2017) 377–385, doi:10.1016/j.nanoen.2016.11.043.
[38] M. Wood, J. Li, Z. Du, C. Daniel, A.R. Dunlop, B.J. Polzin, A.N. Jansen, G.K. Krumdick, D.L. Wood, Impact of secondary particle size and two-layer architectures on the high-rate performance of thick electrodes in lithium-ion battery pouch cells, J. Power Sources. 515 (2021) 230429, doi:10.1016/j.jpowsour.2021.230429.
[39] E. Ayerbe, M. Berecibar, S. Clark, A.A. Franco, J. Ruhland, Digitalization of battery manufacturing: current status, challenges, and opportunities, Adv. Energy Mater. (2021) 2102696, doi:10.1002/aenm.202102696.